Article | Received 12 June 2026; Revised 20 July 2026; Accepted 31 July 2026; Published 25 August 2026
https://doi.org/10.55092/ae20260006

A mechanism-data fusion framework for process-microstructure prediction and optimization in laser directed energy deposition of Ti-6Al-4V using dual-level surrogate modeling

Yushuang Zhang[1,†], Tong Zhao[1,†], Pengwei Liu[1,2,*], Xuanmu Zhou[1], Xintong Wang[1], Jiale Yang[1], Zhuo Wang[3], Xingang Liu[1], Yingjie Zhao[1] and Wenhua Yang[4,*]

[1] School of Mechanical Engineering, Yanshan University, Qinhuangdao, China
[2] National-Local Joint Engineering Research Center for Advanced Manufacture Forming Technology and Equipment, Yanshan University, Qinhuangdao, China
[3] Department of Mechanical Engineering, University of Michigan-Dearborn, Dearborn, USA
[4] Department of Mechanical Engineering, Roy G. Perry College of Engineering, Prairie View A&M University, Prairie View, USA

† These authors contributed equally to this work.

* Correspondence authors; E-mails: pwliu@ysu.edu.cn (P.L.); weyang@pvamu.edu (W.Y.).

Highlights:

- A multiphysics model combining FEM and PFM was established to investigate β grain evolution of Ti-6Al-4V in the L-DED process.
- By integrating multiphysics model with a dual-level LSTM surrogate model, a predictive framework was established for microstructure evolution prediction.
- The accuracy of the framework in predicting thermal and microstructural evolution was validated against physical simulations and experimental measurements.
- The surrogate framework enables rapid microstructure prediction and process optimization.

Abstract: The laser-directed energy deposition (L-DED) process involves complex thermal and material interactions, posing challenges for controlling microstructural evolution in metal additive manufacturing. To enable rapid, efficient process optimization, this study develops a physics-informed mechanism-data fusion framework that couples macroscopic finite element method (FEM) and microscopic phase-field method (PFM) with a dual-level long short-term memory (LSTM) neural network. A multiscale physical model is employed to investigate grain growth behavior and the influence of process parameters on microstructural morphology. To map this non-linear temporal evolution, a dual-level data-driven surrogate model is developed. Compared to a conventional multilayer perceptron (MLP), the LSTM effectively captures time-dependent thermal accumulation. In recursive predictions, four initial input layers were identified as the optimal initialization length, enabling stable

prediction and mitigating potential layer-wise error propagation, maintaining average R^2 values of around 0.95. Using the average grain area as the primary microstructural control target, and incorporating the average grain width, a parameter range of 500–550 W and 13–14 mm/s was identified for achieving near-equiaxed β grains. The proposed framework is implemented as a modular computational pipeline that integrates finite element, phase-field, and surrogate models for reusable and extensible process-microstructure prediction in metal additive manufacturing.

Keywords: laser-directed energy deposition; long short-term memory network; phase-field method; microstructure evolution; simulation optimization

1. Introduction

Laser-directed energy deposition (L-DED) is an additive manufacturing (AM) process that utilizes a high-power laser to melt metal powders and deposit materials layer-by-layer [1]. Compared to selective laser melting (SLM), L-DED offers higher deposition efficiency, greater process flexibility, and lower production costs. As a result, L-DED has found widespread applications in rapid prototyping [2,3], functionally graded materials [4], and the repair of high-value components such as turbine engine blades [5], demonstrating significant industrial potential.

Ti-6Al-4V alloy has become a core structural material in aerospace, marine engineering, and medical applications due to its high specific strength, excellent corrosion resistance, biocompatibility, and thermal stability [6,7]. In aerospace, replacing conventional aluminum alloys and steels with Ti-6Al-4V significantly reduces structural weight and improves fuel efficiency. For instance, it is commonly used in landing gears and engine components [8]. In marine environments, the formation of a stable passive film confers outstanding corrosion resistance, making it an ideal candidate for seawater hydraulic systems and deep-sea equipment [9,10]. On the other hand, the advancement of AM processes such as laser powder bed fusion and electron beam melting has further expanded the applicability of Ti-6Al-4V to complex-shaped components, enhancing both forming efficiency and performance adaptability [11,12].

In L-DED processes, the microstructural control of Ti-6Al-4V alloys is crucial to improving their comprehensive mechanical properties. Current studies mainly focus on the influence of process parameters [13], the optimization of microstructure morphology [14], and post-processing strategies [15,16]. Despite various methods in microstructural control, establishing explicit and reliable process-structural-property relationships remains a significant challenge. The complexity primarily stems from pronounced thermophysical phenomena, such as heat transfer, melt pool flow, and rapid solidification [17,18]. Meanwhile, the high cost of experimental investigations further complicates the validation of these processes. Consequently, various physics-based and data-driven methods have been developed to predict grain structure evolution and guide AM optimization. Recently, these physical models have evolved from conventional single-scale approaches to multiscale frameworks integrating macroscopic and microscopic mechanisms [19,20]. Zhang *et al.* [21] combined the finite element method (FEM) and cellular automata (CA) to simulate thermal histories and microstructure evolution in L-DED, considering heterogeneous nucleation and dendritic growth orientations. Wang *et al.* [22] coupled phase-field modeling phase-field method (PFM) and FEM to study the evolution of solidification microstructures in IN718 alloy during AM, showing that the specific thermal gradient and the preferred crystalline orientation promote niobium enrichment while reducing the long-chain morphologies of

Laves phase formation. However, such multi-scale physics-based simulations are computationally expensive, limiting their application in process window optimization.

Data-driven methods can rapidly construct surrogate models based on a large number of representative samples to approximate the true solution, thereby avoiding the direct establishment of underlying physical relationships [23–26]. Compared with conventional computational approaches that rely on physical constitutive models, these methods can drastically reduce computation time and maximize the efficiency of process development and simulation [27–29]. Multilayer perceptron (MLP) [30], Kriging surrogate modeling [31], Gaussian process regression [32], convolutional neural networks (CNNs) [33], and long short-term memory (LSTM) networks [34] have been increasingly applied to the study of AM processes. However, different methods exhibit distinct capabilities. CNNs are effective for spatial feature extraction but limited in capturing temporal dependencies, while Transformer models and physics-informed neural networks (PINNs) often require high computational cost or face convergence challenges in complex multiscale problems. In contrast, LSTM networks are well-suited for modeling sequential thermal histories, making them more appropriate for describing the dynamic relationships among process, temperature, and microstructure evolution. Recent studies have attempted to couple physics-based models with data-driven approaches to improve prediction accuracy while maintaining the physical interpretability of the models. For example, Kamat *et al.* [35] developed a multiphysics framework integrating thermodynamics, process simulations, and cellular automaton (CA) modeling to analyze melt pool dynamics and grain morphology, which was further used to train surrogate models for predicting microstructural statistics. Wang *et al.* [36] proposed a physics-informed multi-level data-driven framework that links process parameters, thermal history, microstructure evolution, and mechanical properties using FEM, Kriging models, and Monte Carlo simulations. Nevertheless, existing frameworks still exhibit limitations in coupling macroscale thermal behavior with microstructure evolution, capturing the temporal dependencies induced by complex thermal histories, and providing modular and extensible implementations for efficient reuse and integration.

This work presents a mechanism-data fusion framework for predicting β grain microstructure evolution of Ti-6Al-4V alloy in the L-DED process. Unlike conventional data-driven approaches that rely solely on experimental or simulation datasets, the proposed framework integrates FEM and PFM, with a dual-level surrogate model based on an LSTM network. Specifically, the first level establishes a macroscopic thermal surrogate model that maps processing conditions to thermal responses, while the second level develops a microstructure prediction surrogate model that maps thermal histories to microstructural statistics. By embedding features, including laser power, scanning speed, thermal simulation data, average grain area, and time variables extracted from physics-based simulations into the LSTM training process, the model achieves high prediction accuracy while significantly reducing computational cost. The resulting framework enables efficient evaluation of process-temperature-microstructure relationships and supports process optimization. Furthermore, it provides a modular and extensible computational pipeline for process-microstructure prediction in metal additive manufacturing.

2. Experiment

The Ti-6Al-4V powders were deposited on a rolled titanium alloy substrate by the L-DED process. The L-DED forming equipment primarily consists of a six-axis robotic system, a laser generation system, a powder delivery system, and an atmosphere control system [37]. Figure 1 illustrates the schematic diagram of this process. The upper section represents the deposited layers, with the printed sample of 40 mm × 15 mm × 15 mm, while the lower section is the substrate. Each layer follows an alternating scanning strategy, as shown in Figure 1b, and the scanning direction remains the same for adjacent layers. The process parameters were selected with a laser power of 600–700 W and a scanning speed of 8–12 mm/s. Table 1 presents the parameter combinations used in the L-DED process.

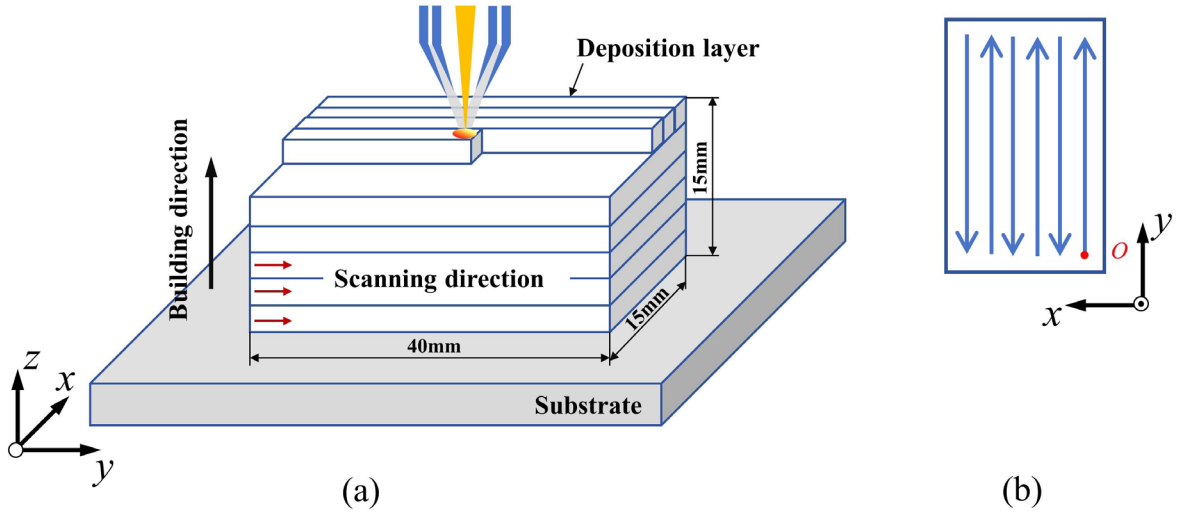

Figure 1. The schematic diagram of the L-DED process. **(a)** L-DED processing; **(b)** Laser scanning path.

Table 1. L-DED Ti-6Al-4V alloy process parameters.

Laser Power (W)	Scanning speed (*v*, mm/s)	Spot diameter (r, mm)	Layer thickness (h, mm)	Hatch spacing (t, mm)	Energy absorption rate
600, 700	8, 10, 12	0.75	0.3–0.5	0.25	0.3

The chemical composition of Ti-6Al-4V is shown in Table 2. The metal powder exhibits high sphericity and a uniform particle size distribution, with an average particle size of 68 ± 5 μm. Before the L-DED experiments, the powder was dried in a vacuum heating oven.

Table 2. Chemical composition of Ti-6Al-4V powder (wt.%).

Al	V	Fe	C	N	H	O	Ti
6.36	4.30	0.031	< 0.01	0.0067	0.0022	0.072	Balance

Optical micrograph (OM) observations were carried out on longitudinal-section samples after mechanical polishing and etching with Kroll's reagent. The samples were also ground and polished using a SiO_2 suspension before electron backscatter diffraction (EBSD) tests at an accelerating voltage of 15 kV.

3. Multiscale physical simulations and data-driven surrogate framework

3.1. Framework overview

As shown in Figure 2, the mechanism-data fusion framework integrating a finite element thermal model and grain growth PFM is constructed in the following three steps:

Step 1: Based on the highly dynamic temperature field and thermal accumulation characteristics during the AM process, a multiscale physical model is developed. The FEM is adopted to calculate the transient temperature histories under different process parameters, which are subsequently imported into the PFM to simulate the dynamic evolution of β grain microstructure. Combined with experimental characterization results for model validation, a large number of high-fidelity sample data covering different process conditions are generated to construct the training and test datasets for subsequent data-driven modeling.

Step 2: Based on the datasets generated by the multiscale physical models, a dual-level, data-driven model is developed to approximate the computationally expensive FEM-PFM simulations. The process parameters, deposition time, and thermal/grain characteristic variables are taken as input features to realize the mapping from processing conditions to thermal response and microstructural features. Specifically, macroscopic thermal surrogate model learns the relationship between process parameters and thermal responses, providing efficient predictions of thermal features. The microstructure prediction surrogate model further establishes the nonlinear mapping between thermal histories and microstructural statistics, enabling rapid prediction of grain evolution.

Step 3: The data-driven model is employed to predict the microstructural evolution of grains during the AM process. Through a systematic analysis of the effects of various process parameters on the layer-wise average grain area, the relationship between processing conditions and microstructure is established. The optimal process window for obtaining near-equiaxed grains is determined, providing an efficient numerical tool for rapid process optimization and microstructure control of L-DED Ti-6Al-4V alloy.

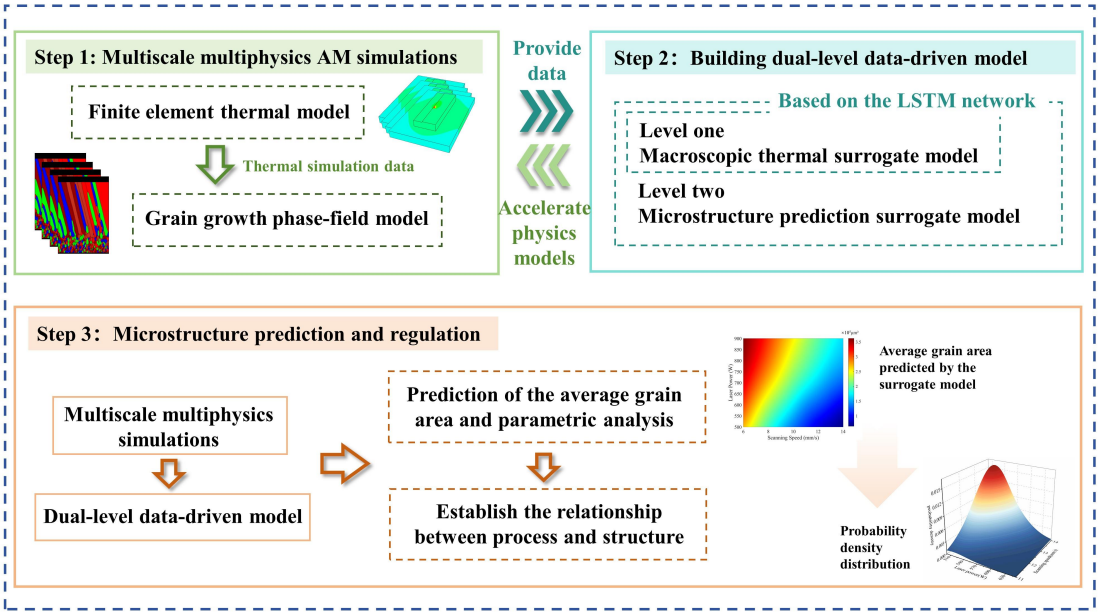

Figure 2. The proposed mechanism-data fusion framework for the L-DED process, comprising multiscale physical modeling, dual-level data-driven modeling, and microstructure prediction and analysis. Process parameters are used to generate FEM thermal histories and PFM β grain evolution data, which are subsequently used for surrogate model prediction and process window identification.

3.2. Multiscale multiphysics methods

3.2.1. Finite element model

During the L-DED process, the conditions affecting the evolution of its temperature field are quite complex, involving powder melting, convective heat transfer, radiative heat loss, and solidification of the molten pool, as well as other intricate phenomena [38]. However, limited computational resources and immature simulation software prevent full consideration of all influencing factors. Therefore, the forming process can be simplified to a transient heat conduction problem:

$$\frac{\partial\left(\rho h(T)\right)}{\partial t}+\nabla\left(k\left(\nabla T\right)\right)=Q(x,y,z) \tag{1}$$

where ρ is the material density; $h(T)$ is the specific enthalpy of the system; k is the thermal conductivity; and Q is the heat flux density. In the single-phase region, $h(T)$ is defined as the specific heat capacity, *i.e.*, $C_p = dh / dT$. In the solid-liquid coexistence region, it is defined as the mass-weighted average value of $h(T)$ for each phase. The thermophysical properties of the Ti-6Al-4V alloy are presented in Table 3 [38–41].

Table 3. Thermophysical properties of Ti-6Al-4V alloy [38–41].

Symbol	Value	Unit
Density	4420	$kg{\cdot}m^{-3}$
Solid line temperature	1877	K
Liquidus temperature	1923	K
Latent heat of phase transformation	286,000	J/kg
Coefficient of heat conduction	14.16	$W{\cdot}m^{-1}{\cdot}K^{-1}$
Specific heat capacity	546	$J{\cdot}kg^{-1}{\cdot}K^{-1}$
β phase transformation temperature	1268	K
Enthalpy of fusion	3.71×10^{4}	$J{\cdot}mol^{-1}$
Solute diffusion coefficient	9.5×10^{-9}	$m^2{\cdot}s^{-1}$

The L-DED begins from the substrate and proceeds layer-by-layer in an upward direction. Each time the laser beam completes a scan on the substrate, a new path is deposited. The laser beam then continues scanning based on this newly formed path. A moving laser heat source is employed to simulate the deposition process, as illustrated in Figure 3. The laser energy input is approximated by a Gaussian heat source, expressed as:

$$Q=\frac{-2\eta P}{\pi R_{laser}^2}\exp\left(\frac{-2\left(x^2+\left(y-v\cdot t\right)^2\right)}{R_{laser}^2}\right) \tag{2}$$

where η represents the energy absorption efficiency; P denotes the laser power; R_{laser}, v, and t correspond to the radius of the laser heat source, the laser scanning speed, and the printing time.

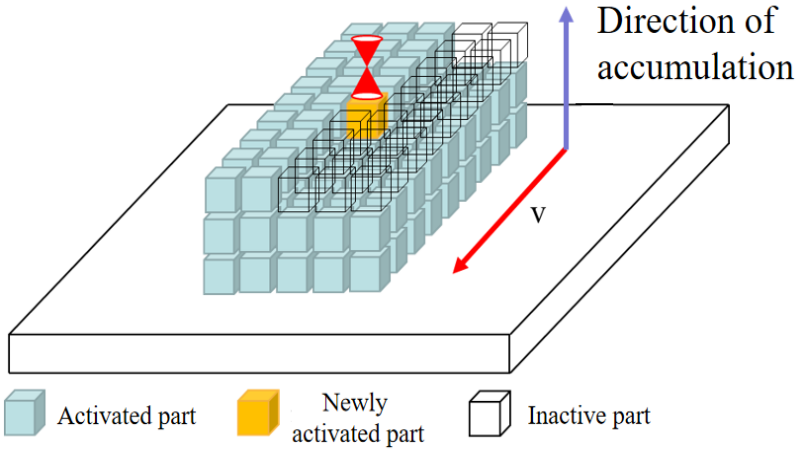

Figure 3. Schematic of the stepwise activation method adopted for numerical simulation of the L-DED process.

The heat loss primarily includes convective heat transfer and radiative heat transfer, which can be expressed as:

$$-k\nabla T = \left[-h\left(T - T_a\right) - \varepsilon_R \sigma_R \left(T^4 - T_a^4\right)\right] \tag{3}$$

where h is the convective heat transfer coefficient, σ_R is the Stefan-Boltzmann constant (5.68×10^{-8} W/m$^2 \cdot$ K^{-4}), ε_R is the surface emissivity, and T_a is the ambient temperature.

3.2.2. Grain growth phase-field model

The macroscopic thermal response is predicted using the FEM described in Section 3.2.1. The temperature field data extracted from the thermal model are imported into the PFM to simulate grain growth on a microscopic scale. The phase-field simulations are performed in a computational domain of 3.0 mm × 5.0 mm. Grain growth during the L-DED process can occur either through epitaxial growth or result from heterogeneous nucleation. When the ratio of the local temperature gradient to the growth rate (G/R) is below a critical threshold [42], nucleation takes place in front of the solid/liquid interface, leading to equiaxed grain formation. Otherwise, grains continue to grow epitaxially. More detailed descriptions of the model can be found in Reference [43].

Pre-existing grains typically grow epitaxially along the direction of the maximum temperature gradient, and this process can be simulated using the time-dependent Ginzburg-Landau equations:

$$\frac{\partial \eta_q(r,t)}{\partial t} = -L_q(T)\frac{\delta F(t)}{\delta \eta_q(r,t)} \quad (q = 1, 2, \ldots, Q) \tag{4}$$

where $\{L_q\}$ are the grain growth kinetic rate coefficients. To account for temperature effects on grain boundary mobility, the temperature T and activation energy ΔE are incorporated into $\{L_q\}$ (Equation (5)):

$$L_q(T) = L_0^* \cdot \left(\frac{T}{T_a}\right)^m \cdot \exp\left(-\frac{\Delta E}{R_g T}\right) \tag{5}$$

where T_a is the ambient temperature, $R_g = 8.314$ J/(mol·K), L_0^* and m ($-1 < m < 1$) are constants.

To account for the influence of the layer-by-layer deposition pattern in the L-DED process on grain growth behavior, a region containing n randomly oriented equiaxed grains is pre-defined in the substrate

before deposition. New powder layers are then periodically added at fixed time intervals. According to the continuous heterogeneous nucleation model, the number of nucleation sites is determined by the maximum nucleation density and the size of the simulation domain, and potential nucleation sites are randomly selected [44]. The nucleation undercooling is introduced to define grain nucleation. The total undercooling ΔT consists of solute undercooling ΔT_c, thermal undercooling ΔT_t, and curvature undercooling ΔT_r, as expressed by the following Equation (6):

$$\Delta T = \Delta T_c + \Delta T_t + \Delta T_r = mC_0(K-1)\left[\frac{I_V(P_C)}{1-(1-k)I_V(P_C)}\right] + \frac{\Delta h_V}{c_p} I_V(P_t) + \frac{2\Gamma}{r} \tag{6}$$

where m is the liquidus slope, k is the solid/liquid partition coefficient, Δh_V is the enthalpy of fusion per unit volume, Γ is the Gibbs-Thomson coefficient, $I_v(P_c)$ is the Ivantsov function, P_c and P_t are the solutal and thermal Peclet numbers, respectively. A Gaussian distribution function is employed to characterize the nucleation density by Equation (7):

$$n(\Delta T) = \int_0^{\Delta T} \frac{dn}{d\Delta T'} d\Delta T' = \int_0^{\Delta T} \frac{n_{\max}}{\Delta T_\sigma \sqrt{2\pi}} \exp\left[-\frac{1}{2}\left(\frac{\Delta T' - \Delta T_N}{\Delta T_\sigma}\right)\right] d\Delta T' \tag{7}$$

where ΔT_N and ΔT_σ represent the average undercooling and the standard deviation of the undercooling, respectively, and $n_{\max}$ is the maximum nucleation site density. The nucleation probability for each grain is given by Equation (8):

$$P_V = \delta n_V V_{ea} = \left\{ n\left[\Delta T(t)\right] - n\left[\Delta T(t-\Delta t)\right] \right\} dx^3 \tag{8}$$

where $V_{ea} = dx^3$ is the effective volume of each lattice point. At each time step, a random number r_a in the range of [0, 1] is generated within the mushy zone, and a new nucleus is formed at the points where $r_a \le P_V$.

In the PFM of grain growth, the material properties of Ti-6Al-4V influence the temperature field distribution in the local regions during printing. It should be noted that the current thermal model allows us to capture the transient temperature field at each micro time step Δt during the AM process. However, a fully coupled simulation of the macroscopic temperature field and the microscopic grain growth PFM is computationally prohibitive. The PFM domain was extracted from the central x-z cross-section of the deposited track, with the high-temperature region defined as the area where the temperature exceeded the β-transus temperature. Regions below T_β were considered to have a negligible effect on β grain evolution. The FEM temperature field was mapped onto the phase-field grid using two-dimensional linear interpolation. Latent heat was included in the thermal model, so the effect of phase transformation on temperature evolution was partially considered at the FEM level. The framework employs a sequential one-way FEM-PFM coupling strategy to balance computational efficiency and physical fidelity.

3.3. Long short-term memory networks

The LSTM networks were originally designed to address the problem of long-term dependencies in neural networks [45]. Traditional recurrent neural networks (RNNs) often struggle with short-term memory and suffer from issues such as gradient vanishing or gradient explosion when processing long sequence data [46,47]. This limits their ability to capture and utilize distant dependencies. In contrast, LSTM networks incorporate a cell state within their recurrent structure, which enables selective retention

and forgetting of information. This allows them to learn and preserve long-term dependencies effectively. Consequently, LSTM networks are particularly advantageous for tasks involving time series and predictive modeling, such as the prediction of microstructure evolution during grain growth [48,49] and thermal field prediction [50]. Furthermore, they exhibit strong generalization and robustness capacities, making them well-suited for integration with the multiphysics models discussed in this study.

The LSTM structure is mainly composed of several gating units and a memory unit. The gating units serve as checkpoints that control the selective flow of information. There are three types of gates: the input gate, the forget gate, and the output gate. The data entering the gates is regulated by a σ function, which outputs values in the range [0, 1]. Meanwhile, the tanh function applies a nonlinear transformation to the input or cell state, constraining the output within the range [–1, 1].

In this study, the σ function and the tanh function are defined as follows:

$$\sigma(x) = \frac{1}{1+\mathrm{e}^{-x}} \tag{9}$$

$$\tanh(x) = \frac{2}{1+\mathrm{e}^{-2x}} - 1 \tag{10}$$

Their value ranges are (0,1) and (−1,1), respectively.

The main role of the forget gate is to decide what information to forget or retain when the previous output vector h_{t-1} and the input vector x_t pass through it, and is defined by Equation (11):

$$f_t = \sigma\left(W_f \cdot \left[h_{t-1}, x_t\right] + b_f\right) \tag{11}$$

where f_t, W_f, and b_f represent the output value of the forget gate, the weight matrix, and the bias, respectively.

Like the forget gate, the input gate also passes a certain proportion of the current input x_t to the cell state C_t. This process is shown in Equations (12)–(14):

$$i_t = \sigma\left(W_i \cdot \left[h_{t-1}, x_t\right] + b_i\right) \tag{12}$$

$$\tilde{M}_t = \tanh\left(W_C \cdot \left[h_{t-1}, x_t\right] + b_C\right) \tag{13}$$

$$C_t = f_t \cdot C_{t-1} + i_t \cdot \tilde{M}_t \tag{14}$$

where i_t represents the data passed by the input gate, $\tilde{M}_t$ indicates the cell state value at the current time step.

The output gate controls how much of the current cell state C_t is output together with the hidden state h_t. This process is described by Equations (15) and (16):

$$o_t = \sigma\left(W_o\left[h_{t-1}, x_t\right] + b_o\right) \tag{15}$$

$$h_t = o_t \cdot \tanh\left(C_t\right) \tag{16}$$

where, o_t, W_o, and b_o represent the output value of the output gate, the weight matrix, and the bias term, respectively, similar to those of the forget gate and input gate.

3.4. Evaluation metrics

In this paper, the root mean square error (RMSE), relative error (RE), and coefficient of determination (R^2) are used to assess the prediction accuracy of the data-driven model, which are expressed as:

$$\mathrm{RMSE} = \sqrt{\sum_{i=1}^{n} \frac{(\hat{y}_i - y_i)^2}{n}} \tag{17}$$

$$\mathrm{RE} = \frac{1}{n} \sum_{i=1}^{n} \left| \frac{(\hat{y}_i - y_i)}{y_i} \right| \tag{18}$$

$$\mathrm{R}^2 = 1 - \frac{\sum_{i=1}^{n} (\hat{y}_i - y_i)^2}{\sum_{i=1}^{n} (\bar{y} - y_i)^2} \tag{19}$$

The RMSE quantifies the differences between the predicted values and the actual measurements; the smaller the RMSE, the more precise the predictions. The RE is the absolute error between the predicted and actual values, normalized by the average of the actual measurements. Its value ranges from 0 to 1. The R^2 primarily assesses the explanatory power of the predictive model. Values closer to 1 indicate a better fit for the model. These metrics collectively provide a comprehensive evaluation of the model's performance in capturing the underlying patterns of the data.

3.5. Network parameters and feature mapping

The proposed mechanism-data fusion framework includes a macroscopic thermal surrogate model and a microstructure prediction surrogate model, as illustrated in Figure 4. During training, simulation results from multiscale physical models are utilized to train the two surrogate models. All data is divided into training and testing sets at an 8:2 ratio, with the input features normalized using the min-max method. Model accuracy is quantitatively assessed using R^2, RMSE, and RE.

- Input: Different physical input features were employed for the thermal and microstructure surrogate models. For the thermal surrogate model, the input variables include the FEM thermal simulation data T_s, P, v, and deposition time t. For the microstructure surrogate model, the input variables consist of the average grain area A_s, P, v, and t.
- Hidden units: The number of units in the hidden layer of the LSTM model. 15 units are included in the developed LSTM model.
- Epochs: The number of times that the model iterates over the entire training dataset during the training process. The number of training iterations is set to 4800 for the thermal surrogate model and 200 for the microstructure surrogate model. These values were selected based on preliminary experiments conducted with Keras Tuner and monitored through early stopping strategies to ensure convergence without overfitting.
- Output: In the thermal surrogate model, the LSTM networks predict the temperature field distribution Tt; whereas in the microstructure prediction surrogate model, the output is the average grain area A.
- Mini-batch size: A total of 128 samples are used for each parameter update during training.
- Learning rate: The step size at which the parameters are updated during training. The initial learning rate is set to 0.001. Moreover, a piecewise learning rate scheduling strategy was implemented. For

the thermal surrogate model, the learning rate is reduced by a factor of 0.1 every 400 epochs; for the microstructure surrogate model, the learning rate was reduced by a factor of 0.5 every 80 epochs.

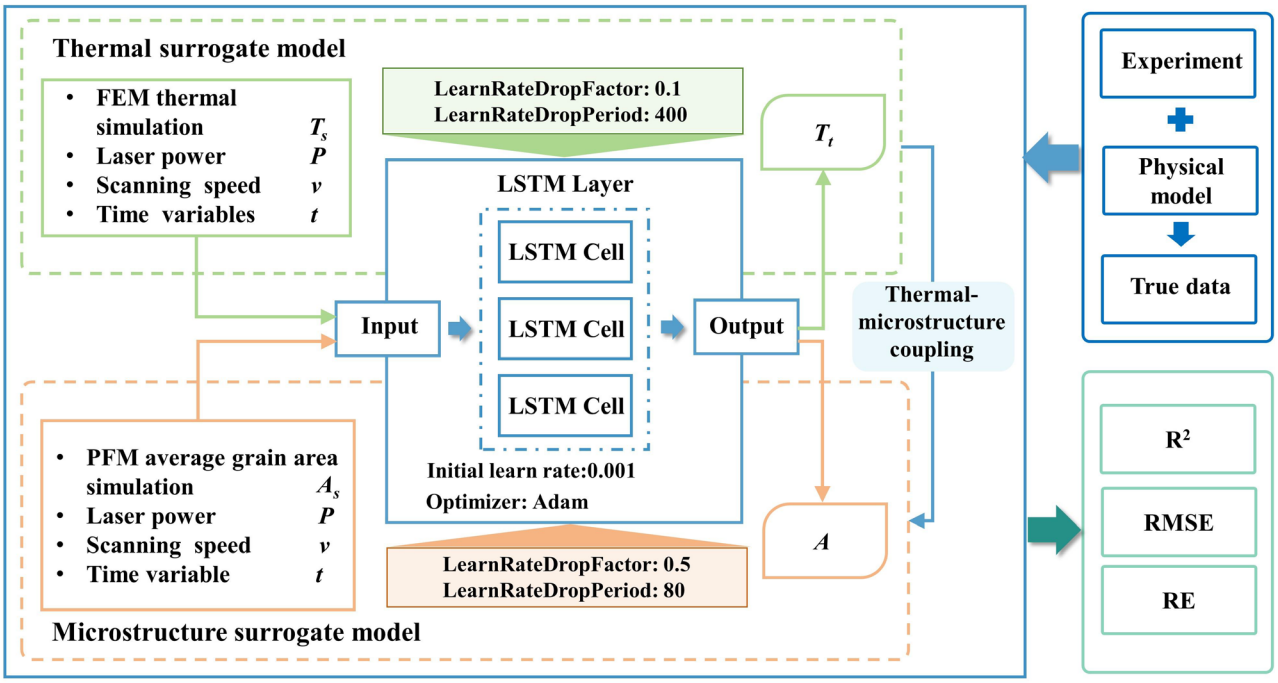

Figure 4. Training framework of the dual-level data-driven model, consisting of macroscopic thermal prediction and microscopic microstructure prediction modules.

4. Results and discussion

4.1. Validation of multiscale physics-based models

To validate the accuracy of the multiscale physical model, this study selected specimens fabricated with 600 W and 8 mm/s, as shown in Figure 5. First, a single-track L-DED printing experiment was conducted to validate the reliability of the finite element thermal conduction model. The temperature distribution of the melt pool cross-section at t = 2.5 s was extracted and compared with experimental results. It was found that the melt pool shape in the simulation, defined as the region with a temperature higher than the melting point of Ti-6Al-4V alloy (1923 K), was in good agreement with that obtained from the experiment under the same process parameters, as shown in Figure 5a.

Furthermore, the solidification interface evolution trends of the molten pool cross-section obtained from metallographic image and finite element simulation were compared (Figure 5b). The results show that the trend of the solid/liquid interface from the simulation closely matches the experimental observation, with the melt pool dimensions remaining at approximately 900 μm in width and 700 μm in depth.

At the microstructural scale, the PFM results for the first ten layers were contrasted with the grain morphology observed via EBSD under the same process parameters (600 W, 8 mm/s), as shown in Figure 5c. By analyzing grain growth morphology and grain sizes, the accuracy of the PFM was further evaluated. It clearly shows that both the simulation and experimental observations reveal coarsened columnar β grains epitaxially growing at an angle of approximately 65°. Table 4 presents the dimensions of the columnar grains. The simulated columnar grains had lengths ranging from 170 to 3280 μm and widths from 40 to 345 μm, while EBSD showed grain lengths of 229 to 3070 μm and

widths of 46 to 465 μm. The PFM results demonstrated excellent consistency with EBSD, confirming the reliability of the physics-based models.

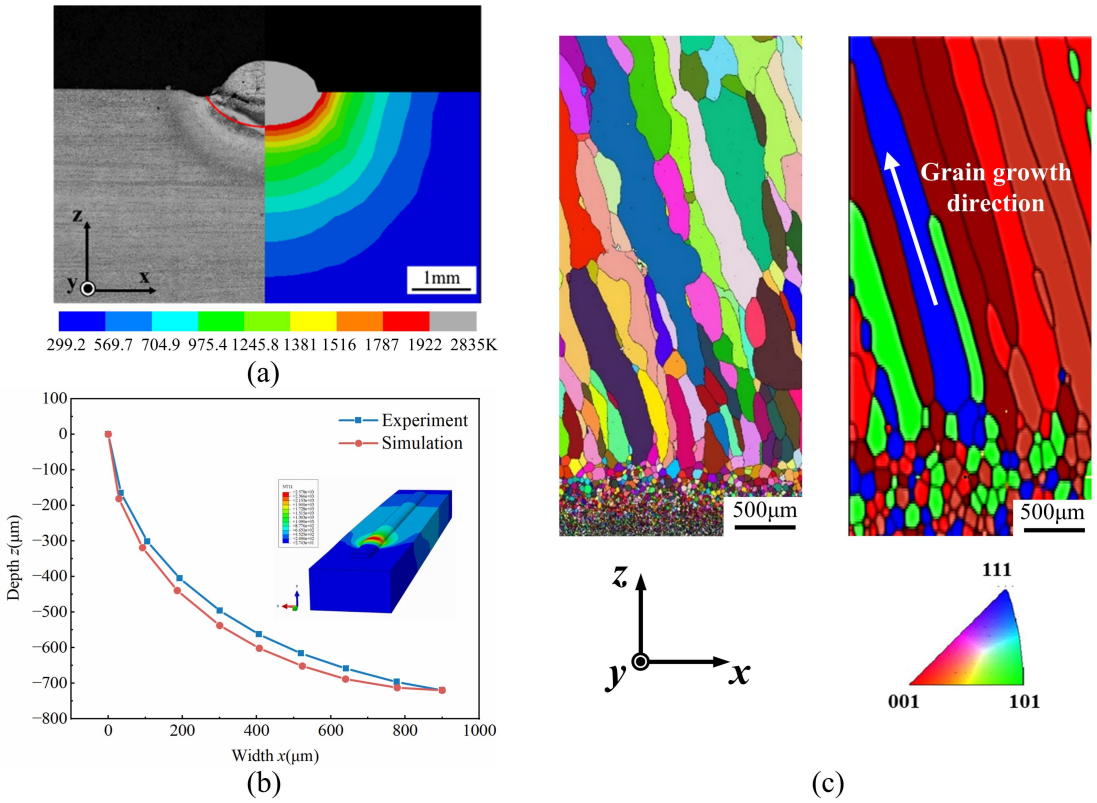

Figure 5. Comparison between experimental and simulation under 600 W laser power and 8 mm/s scanning speed. **(a)** Single-track melt pool morphology; **(b)** Solid-liquid interface morphology; **(c)** β grain structure evolution.

Table 4. Statistical comparison of β grain sizes between EBSD characterization and simulations.

Method	Grain length (μm)	Grain width (μm)
EBSD	229–3070	46–465
Simulation	170–3280	40–345

4.2. Effect of process parameters on the microstructure in L-DED

In the L-DED process, replacing coarsened epitaxial β columnar grains with fine equiaxed structures is vital for enhancing mechanical performance [51–53]. In this section, a multiscale physical model was applied to systematically analyze the evolution of grain structure in L-DED fabricated Ti-6Al-4V alloy under varying laser powers and scanning speeds. Additionally, it provides a validated data generator for the surrogate models to predict grain morphologies.

Figure 6 illustrates the evolution of β columnar grain morphology on the *x*-*z* plane of a Ti-6Al-4V alloy under various processing parameters. In addition to predicting the grain structure, the multiphysics model also reveals the microscopic mechanism of grain growth. The growth process can be divided into several stages:

Stage 1: At the initial stage, the substrate layer is preset with a randomly distributed grain orientation, and the grain morphology mainly consists of fine equiaxed grains. At this stage, the temperature variation across the equiaxed grains of most of the substrate is minimal. However, under

the influence of the macroscopic melt pool, the equiaxed grains begin to grow along the direction of melt pool motion and perpendicular to the melt pool boundary, gradually forming tilted fine columnar grains.

Stage 2: Due to the higher thermal gradient, the initially formed fine columnar grains begin to grow epitaxially. The printing strategy in each layer promotes grain growth tilted toward the *z* direction. During this process, grains gradually achieve preferential growth and consume adjacent finer grains.

Stage 3: Although the epitaxial growth mechanism of columnar grains continues to dominate, their growth in width ceases, and the grains continue to grow along their length. At this stage, the columnar grains exhibit a strong preferential orientation and continuously absorb newly nucleated fine equiaxed grains. The combined effect of these mechanisms leads to the epitaxial growth of tilted columnar grains along the deposition direction, which eventually become dominant in the microstructure.

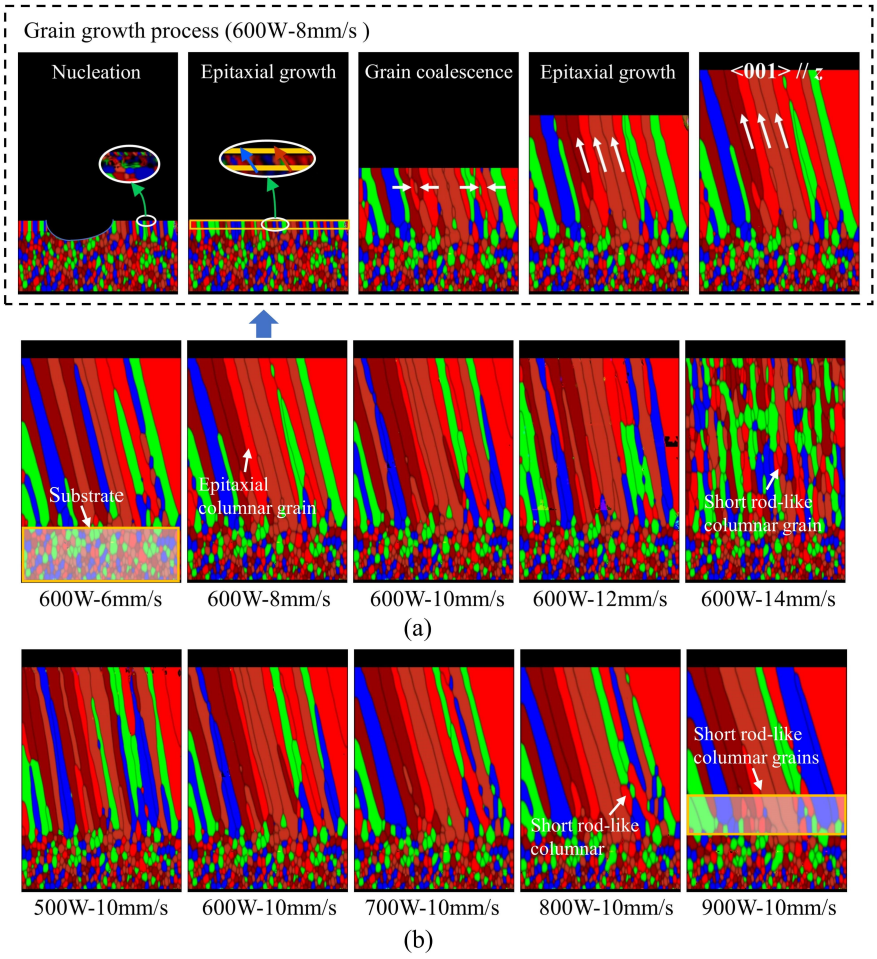

Figure 6. PFM results on the x-z cross section. **(a)** 600 W with different scanning speeds; **(b)** 10 mm/s with different laser powers. The grain growth process under processing parameters of 600 W, 8 mm/s is inserted.

To more clearly describe the evolution of β grains under different processing parameters, the grain aspect ratio λ, total grain count, and average grain area were analyzed for the region above the predefined equiaxed grain substrate. As shown in Figure 7a,c, under a laser power of 600 W, the distribution of λ varies significantly with scanning speed. When the scanning speed is between 6–12 mm/s, λ values are primarily distributed across two distinct intervals between 1–5 and 13–19. The number of grains increases with scanning speed, with a particularly sharp rise at 14 mm/s, where the count jumps from approximately 85 of 12 mm/s to 222, an increase of nearly threefold. Meanwhile, the average grain area decreases with

increasing scanning speed, around 276 × 10^3 μm² at 6 mm/s, dropping to about 42 × 10^3 μm² at 14 mm/s. These trends suggest that higher scanning speeds increase nucleation rates while reducing the likelihood of remelting previously formed grains. This inhibits the continuous epitaxial growth of columnar grains. As a result, grain sizes tend to decrease. Furthermore, at higher scanning speeds, the probability of heterogeneous nucleation between successive layers increases. In contrast, at lower speeds, the epitaxially growing columnar grains tend to consume newly nucleated grains, limiting their development [54].

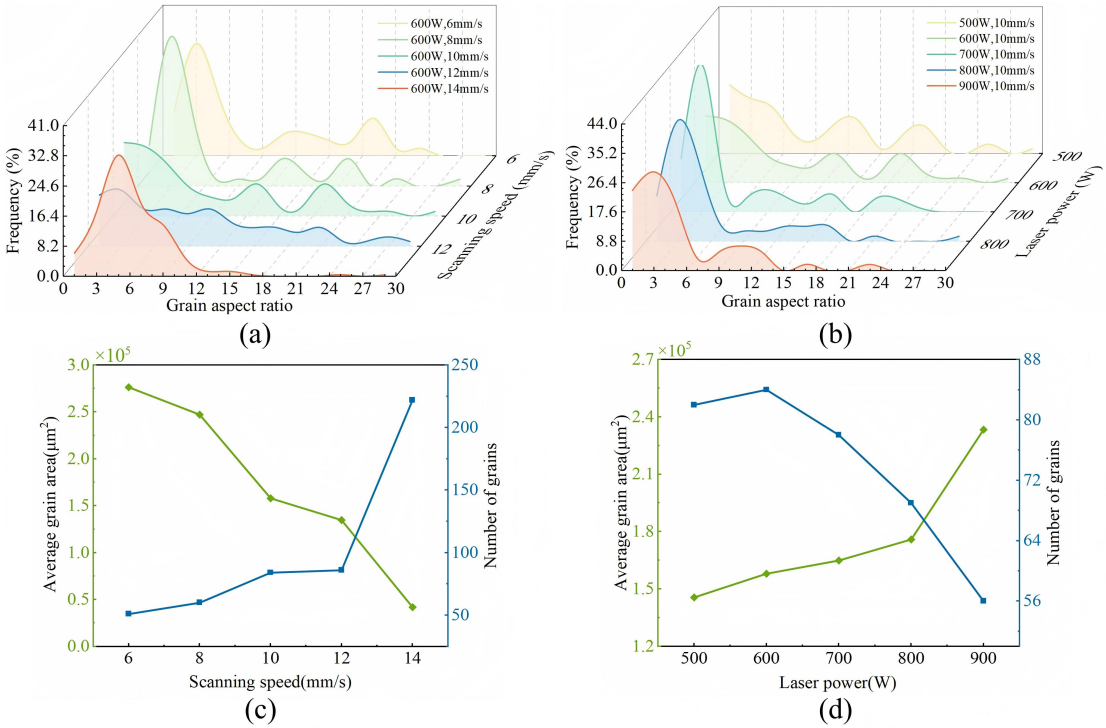

Figure 7. Effect of processing parameters on β grain characteristics. **(a)** Aspect ratio distributions of grains at 600 W under different scanning speeds; **(b)** λ distributions of grains at 10 mm/s under different laser powers; **(c)** Average grain area and total grain number at 600 W under different scanning speeds; **(d)** Average grain area and total grain number at 10 mm/s under different laser powers.

Figure 7b presents the distribution of λ at *v* of 10 mm/s under varying *P* from 500 W to 900 W. Overall, the λ are mainly distributed within the range of 1–5. At the same time, in combination with Figure 6, it can be observed that the short rod-like columnar grains mainly appear at the early stage of printing, where newly nucleated grains begin to grow along the molten pool boundary. At this stage, the thermal gradient within the melt pool is relatively stable, and higher energy input promotes grain formation. However, the competition among grains also intensifies, partially suppressing the continued epitaxial growth of the initially formed columnar grains [55,56]. As shown in Figure 7d, the average grain area increases with rising laser power, from approximately 145 × 10^3 μm² at 500 W to about 233 × 10^3 μm² at 900 W. However, the total number of grains shows a decreasing trend. There is a slight increase at 600 W. While the average grain area increases, the number of grains decreases. This is because higher laser power increases the lateral growth of columnar grains, resulting in coarser epitaxial structures.

4.3. Development and performance evaluation of the surrogate model

4.3.1. Prediction of thermal field and microstructure evolution

To evaluate the capability of the proposed surrogate framework in capturing the process-thermal-microstructure relationship during L-DED, the predictions of the thermal and microstructure surrogate models were compared with the corresponding FEM and PFM simulation results under the processing conditions of 600 W and 8 mm/s. For thermal history prediction, temperature data on the *x-z* cross-section were extracted from the FEM simulation at intervals of 0.5 s during the deposition of the 10th layer, yielding a total of 4000 temperature field data points. These data were then used to predict the temperature distribution on the *x-z* cross-section at t = 4.5 s. Since grain evolution in L-DED is strongly dependent on thermal history, the sequential grain area data were used to characterize the temporal evolution of microstructure. The average grain area was extracted from the PFM simulation every 50 s, resulting in 3000 microstructure data points, which were subsequently used to predict the evolution of the average grain area at 425 s, as shown in Figure 8.

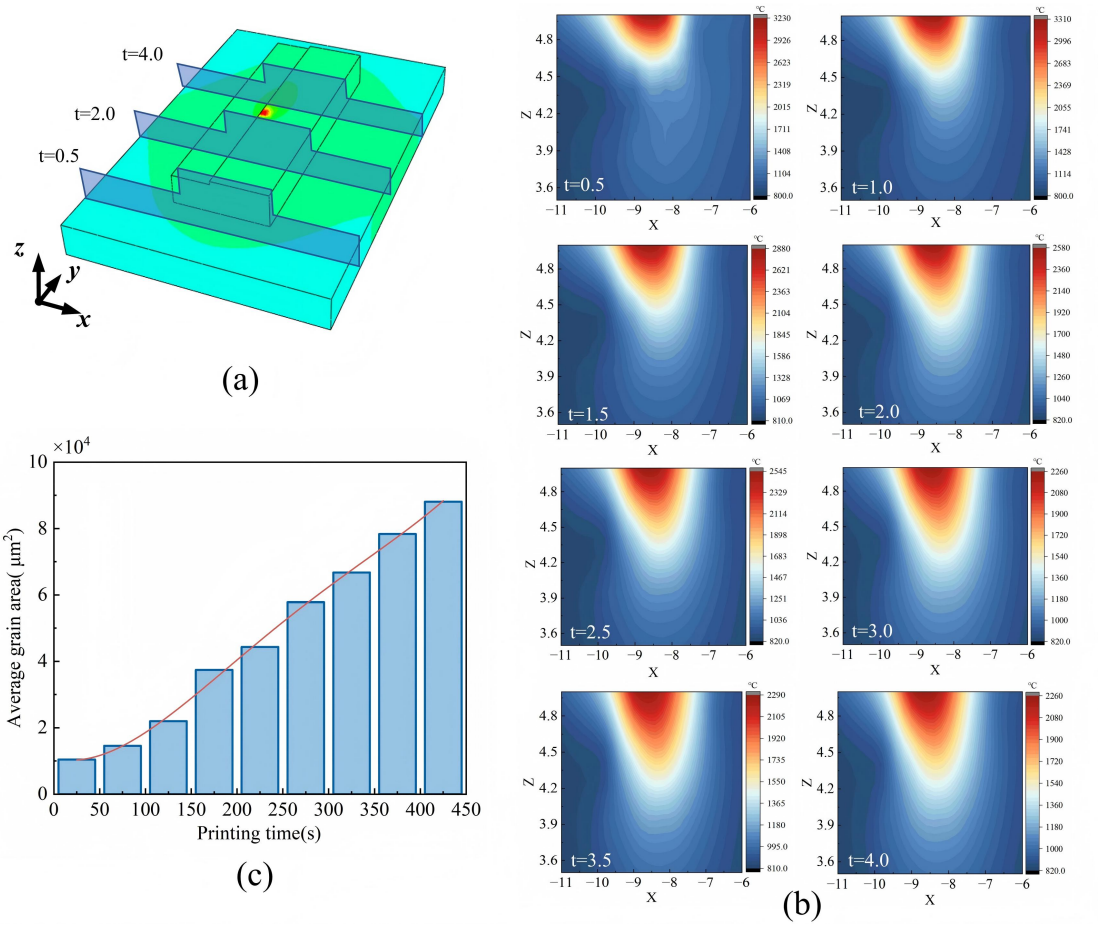

Figure 8. Under the processing conditions of 600 W and 8 mm/s. **(a)** schematic illustration of the extraction of temperature field data from the x-z cross-section at different time instants; **(b)** temperature field data extracted on the x-z cross-section from 0.5 s to 4.0 s; and **(c)** average grain area extracted every 50 s over the time range of 25 s to 425 s.

As shown in Figure 9, the predicted values exhibit agreement with the simulation data, with most data points distributed closely around the $y = x$ line. However, in the region with larger values, the

prediction accuracy decreases due to the relatively small number of samples, resulting in certain deviations between the predicted and actual values. A further quantitative analysis of the prediction errors is presented in Table 5. The thermal surrogate model achieves an R^2 of 0.96, an RE of 3.78%, and an RMSE of 73.89 K that the model maintains a small overall error across the prediction range and can stably and accurately predict the thermal response. The microstructural surrogate model achieves an R^2 of 0.95, an RE of 12.46%, and an RMSE of 165.34 μm², indicating a certain degree of fluctuation and error in predicting grain size. This may be attributed to the inherently stronger nonlinearity and multiscale nature of grain evolution, which are difficult to fully capture with a surrogate model, as well as the relatively small proportion of large-grain-size samples in the training dataset, limiting the model's generalization in that range. Overall, both surrogate models exhibit good predictive capability in their respective domains, with particularly reliable performance in data-dense regions.

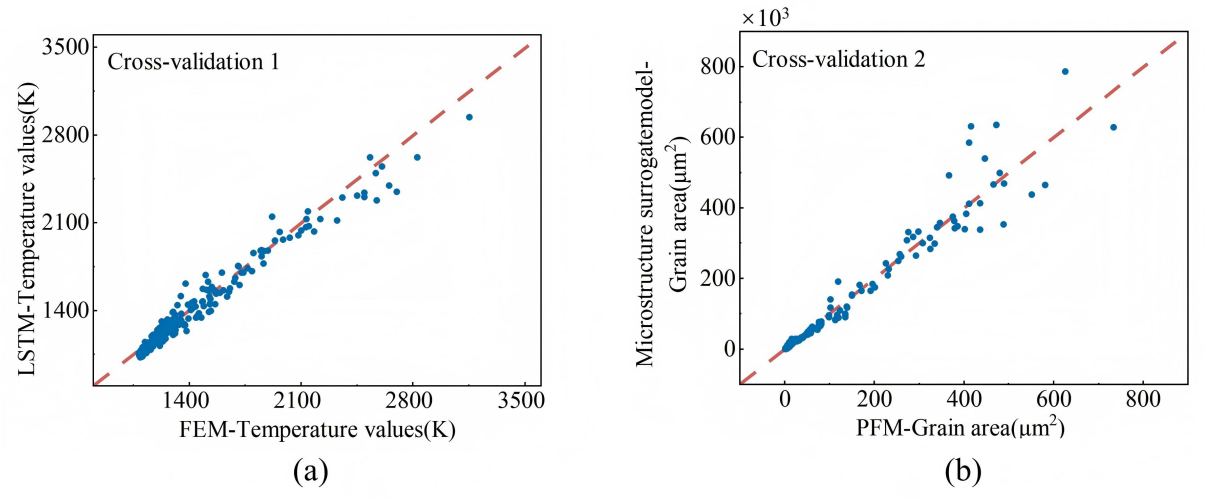

Figure 9. Cross-validation of **(a)** the thermal surrogate model against finite element results and **(b)** the microstructure surrogate model against phase-field results.

Table 5. Prediction error of the thermal surrogate model and microstructure surrogate model.

Model	R^2	RE	RMSE
Cross-validation 1	0.96	3.78%	73.89 K
Cross-validation 2	0.95	12.46%	165.34 μm²

The proposed thermal-microstructure surrogate framework effectively establishes the mapping relationship between process parameters, thermal history, and grain evolution behavior. In this framework, the thermal surrogate model is employed to rapidly reconstruct thermal evolution sequences, which serve as essential input features for subsequent microstructure prediction. The microstructure morphology reconstruction presented in Section 4.3.1 serves as a high-fidelity validation of the proposed framework in capturing grain-scale microstructural features under specific process conditions. The subsequent analyses focus on surrogate modeling of the layer-wise evolution of microstructure,

particularly the average grain area, across multiple processing conditions for recursive prediction and process optimization.

4.3.2. Layer-wise average grain area prediction

Due to the layer-by-layer deposition nature of L-DED, the elapsed printing time varies with scanning speed. To establish a unified temporal representation, the deposition layer number was adopted as the evolution coordinate. Consequently, grain evolution prediction was formulated as a layer-wise sequence forecasting problem. Sixteen process conditions were used for model training, while four unseen process conditions (600 W, 10 mm/s; 600 W, 12 mm/s; 700 W, 10 mm/s; 700 W, 12 mm/s) were reserved for testing to evaluate the generalization capability of the proposed model.

To determine an appropriate initial input sequence length, a sensitivity analysis was conducted using different initialization lengths ranging from 2 to 6 layers. As shown in Figure 10, the prediction performance is dependent on the number of initial input layers. Among all tested configurations, a length of four layers achieved the highest mean R^2 value (0.943 ± 0.015). Moreover, the corresponding standard deviation was the lowest, indicating the most stable prediction performance. Initial input sequences that were too short could not adequately capture the layer-wise thermal accumulation effect and interlayer epitaxial grain growth behavior, thereby providing insufficient historical information for learning the intrinsic grain evolution characteristics. Conversely, excessively long initialization sequences introduced redundant temporal information that can weaken dominant sequential features and reduce the effectiveness of recursive forecasting. Therefore, four initial input layers were selected as the optimal initialization length for subsequent analyses. Based on this result, training adopted a sliding-window one-step forecasting scheme, in which the grain areas of the prior four layers were used to predict the subsequent layer. During testing, the first four layers served as the initial input sequence, enabling recursive prediction of grain evolution over the following eleven layers. By feeding the predicted grain area back into the input sequence at each step, the framework enables evaluation of both long-range prediction and error accumulation behavior during layer-wise microstructure evolution.

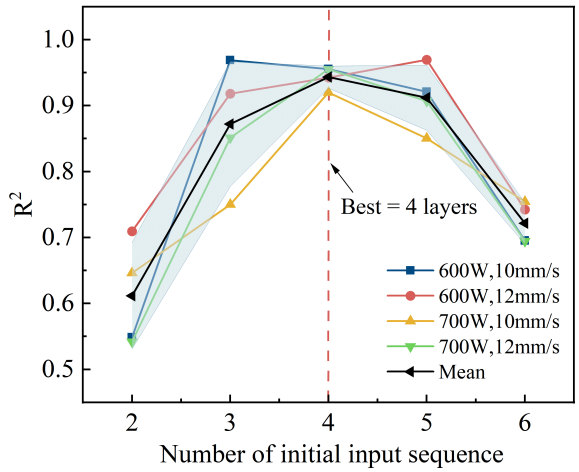

Figure 10. Sensitivity of recursive forecasting performance to initial input sequence length.

Figure 11 compares the layer-wise average grain area predicted by the LSTM and MLP models under four process conditions. The corresponding quantitative evaluation metrics, including R^2, RE, and RMSE, are presented in Figure 12. As observed, the proposed LSTM model accurately captures the

evolution trend of grain growth throughout the entire deposition process. Owing to its recurrent architecture and memory mechanism, the LSTM is capable of learning the temporal dependence between successive deposited layers and preserving the evolution history of the microstructure. Consequently, the model achieves high prediction accuracy across all testing conditions, with average R^2 values around 0.95, average RE values around 8.14%, and RMSE values on the order of 0.85×10^4 μm².

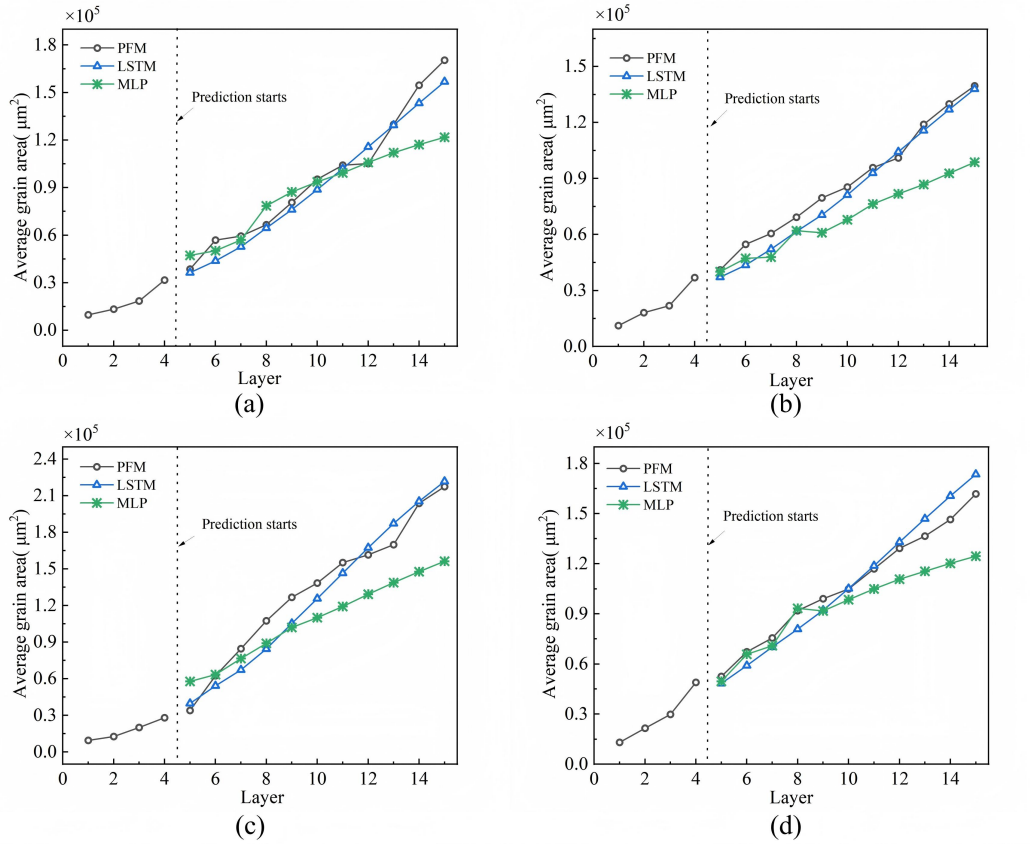

Figure 11. Comparison of layer-wise average grain area predicted by LSTM and MLP with PFM for four process conditions. **(a)** 600 W, 10 mm/s; **(b)** 600 W, 12 mm/s; **(c)** 700 W, 10 mm/s; and **(d)** 700 W, 12 mm/s.

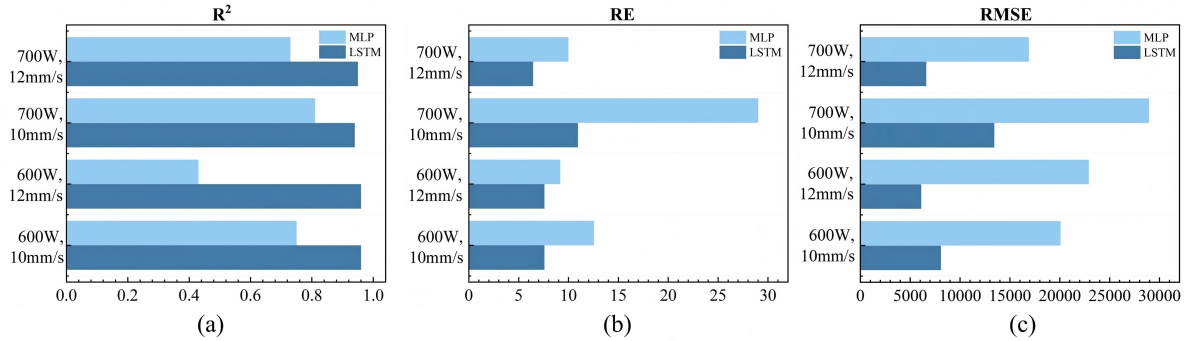

Figure 12. Comparison of prediction accuracy between LSTM and MLP for four process conditions. **(a)** R2; **(b)** RE; **(c)** RMSE.

In contrast, the MLP model exhibits noticeably inferior performance. Although reasonable agreement is achieved during the early deposition stages, the prediction accuracy drops sharply after

the 9th or 10th layer. Specifically, the corresponding R^2 values fluctuate substantially between approximately 0.4 and 0.8, while the average RE increases to about 15% and the RMSE reaches 2.22×10^4 μm². This degradation occurs because the MLP treats the inputs as independent static variables and lacks an explicit mechanism for modeling sequential dependencies; consequently, it cannot effectively capture the cumulative layer-to-layer evolution behavior of grain growth. As a result, the predicted grain areas tend to be systematically underestimated in the later deposition stages. These results demonstrate that incorporating temporal information is essential for accurately describing grain evolution during layer-by-layer deposition, and that the LSTM architecture is more suitable than conventional feedforward neural networks for microstructure sequence forecasting.

To further investigate the effect of error propagation during recursive forecasting, the layer-wise divergence between teacher forcing and recursive forecasting was adopted as an indicator of trajectory drift, as shown in Figure 13. Since the same trained surrogate model generates both strategies, the divergence primarily reflects the cumulative impact of prediction errors fed back. As observed, both the teacher forcing and recursive forecasting errors exhibit layer-dependent fluctuations rather than monotonically increasing behavior. Relatively larger deviations are mainly observed during the early prediction stages, where grain evolution is more sensitive to local thermal-history variations and interlayer growth competition. With increasing deposition layer number, the prediction errors gradually decrease and become more stable, indicating that the grain growth process progressively evolves into a relatively stable thermal accumulation regime. Consequently, the divergence between the two forecasting strategies remains relatively small and does not exhibit continuous growth with increasing layer number. This behavior suggests that the proposed surrogate model can effectively capture the underlying grain evolution dynamics and maintain stable long-range forecasting performance under recursive prediction conditions.

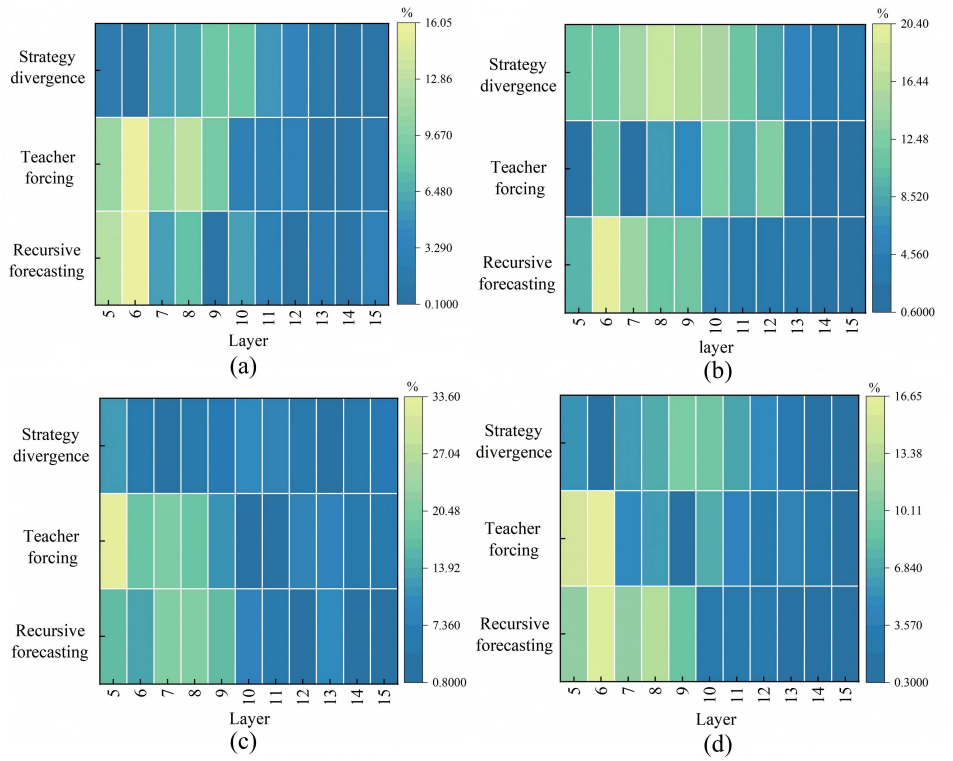

Figure 13. Layer-wise accumulation of prediction errors for teacher-forcing and recursive forecasting, evaluated against the corresponding simulation results under four process conditions. **(a)** 600 W, 10 mm/s; **(b)** 600 W, 12 mm/s; **(c)** 700 W, 10 mm/s; **(d)** 700 W, 12 mm/s.

4.3.3. Computational efficiency and sensitivity analysis

The computational efficiency of the proposed surrogate framework was evaluated by comparing its computational cost with that of the physics-based simulations. For a single process condition, the FEM required approximately 40 h to predict the thermal history, and the subsequent PFM for microstructure evolution required an additional 20 min on an Intel i7 8-core CPU, totaling over 40 h for a complete physical simulation run. In contrast, the training and testing of the proposed surrogate model were highly efficient, requiring only about 10 min once the dataset was prepared. Compared with the multiscale multiphysics simulations, the proposed data-driven framework achieved a computational acceleration of approximately 2.4×10^2 times for new parameter evaluations, successfully reducing the computational cost by more than two orders of magnitude.

Figure 14 illustrates the sensitivity of layer-wise grain area evolution to variations in laser power and scanning speed. For both parameters, the differences between the predicted trajectories of evolution become progressively larger in a non-linear manner as the deposition process continues, suggesting that the effects of variations in the process parameter are continuously accumulated and amplified through successive thermal cycles. As shown in Figure 14a, increasing laser power shifts the grain evolution trajectories upward. The separation between different trajectories is relatively small but gradually enlarges in the later stages. In contrast, increasing scanning speed reduces the grain area, as shown in Figure 14b. These parameter-induced variations in grain size and the underlying physical mechanisms governing solidification and grain growth will be further evaluated alongside the visualized grain morphologies in the subsequent section.

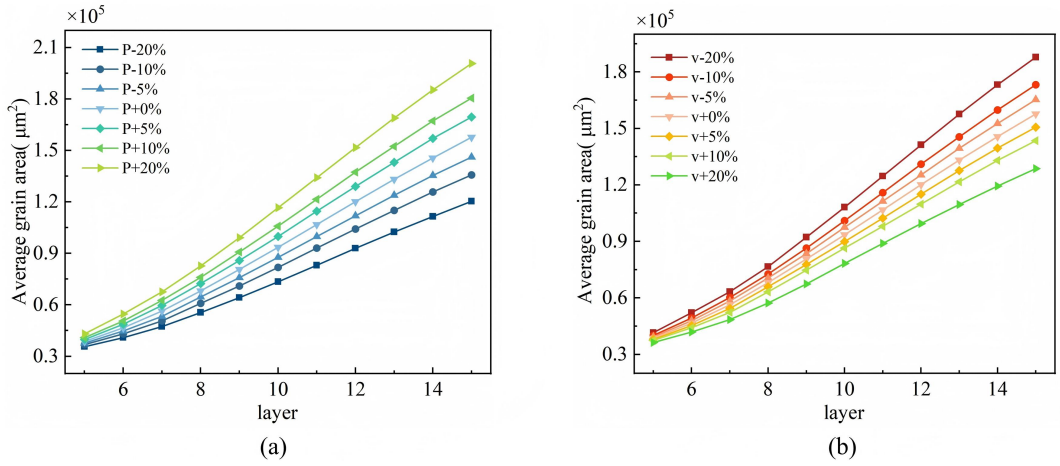

Figure 14. Sensitivity of layer-wise grain area evolution to **(a)** laser power and **(b)** scanning speed variations predicted by the microstructure surrogate model

Furthermore, the trajectory divergence induced by laser power is noticeably larger than that caused by scanning speed, indicating that laser power plays a more dominant role in governing grain evolution during the L-DED process. As further confirmed by the final-layer sensitivity analysis (Figure 15), a ± 20% variation in laser power results in a grain area variation of approximately 50.9% relative to the baseline condition, whereas the corresponding variation induced by scanning speed is only 37.5%. The sensitivity analysis demonstrates that the proposed surrogate model not only provides accurate predictions but also preserves the underlying process-microstructure relationships captured by the physics-based simulations.

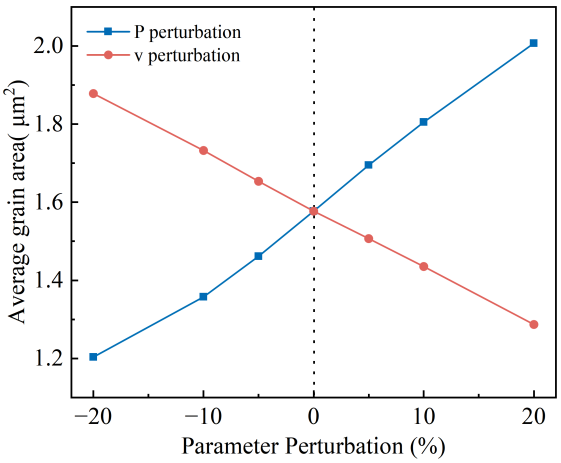

Figure 15. Sensitivity of final-layer grain area to laser power and scanning speed perturbations.

4.4. Surrogate-based microstructure prediction and process optimization

The multiscale physical model results for 20 processing parameter sets were used as inputs to the microstructural surrogate model. The corresponding average grain area was used as the output to construct the prediction network. The predicted β grain morphology of Ti-6Al-4V alloy during the L-DED process is visualized in Figure 16. Specifically, at a constant scanning speed, a higher laser power increases the linear energy density, which enlarges the molten pool and retards the solidification cooling rate, thereby providing a sustained driving force for competitive grain growth and resulting in a larger average grain area. Conversely, increasing the scanning speed restricts the heat source dwell time and accelerates cooling, which effectively suppresses grain coarsening. According to the predicted grain area distribution map, the parameter region with relatively low laser power and high scanning speed yields the smallest grain size. This region is therefore identified as the optimal parameter window for forming near-equiaxed microstructures.

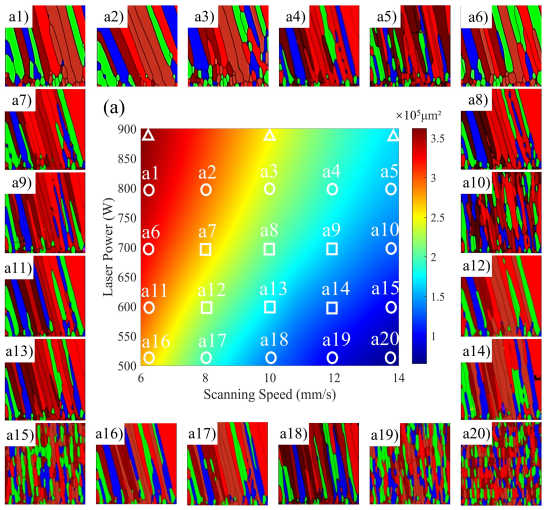

Figure 16. Microstructure surrogate model and PFM results for the L-DED Ti-6Al-4V alloy under different processing parameters. **(a1–a20)** grain morphologies simulated by the PFM for 20 combinations of laser power and scanning speed, providing the average grain areas; and **(a)** surrogate model predicted heatmap illustrating the distribution of the average grain area across different processing windows.

Figure 17 presents the validation results of the proposed surrogate model through experimental measurements and extrapolation assessments. Figure 17a shows the OM obtained under six processing conditions, combining laser powers of 600 W and 700 W with scanning speeds of 8, 10, and 12 mm/s. As shown in Figure 17b, although the LSTM predictions slightly underestimate the measured data, they capture the overall evolution trends. As shown in Table 6, the model achieves an R^2 value of 0.96, an RE of 11.84%, and an RMSE of 1.37×10^4 μm², demonstrating good agreement between the surrogate predictions and experimental measurements.

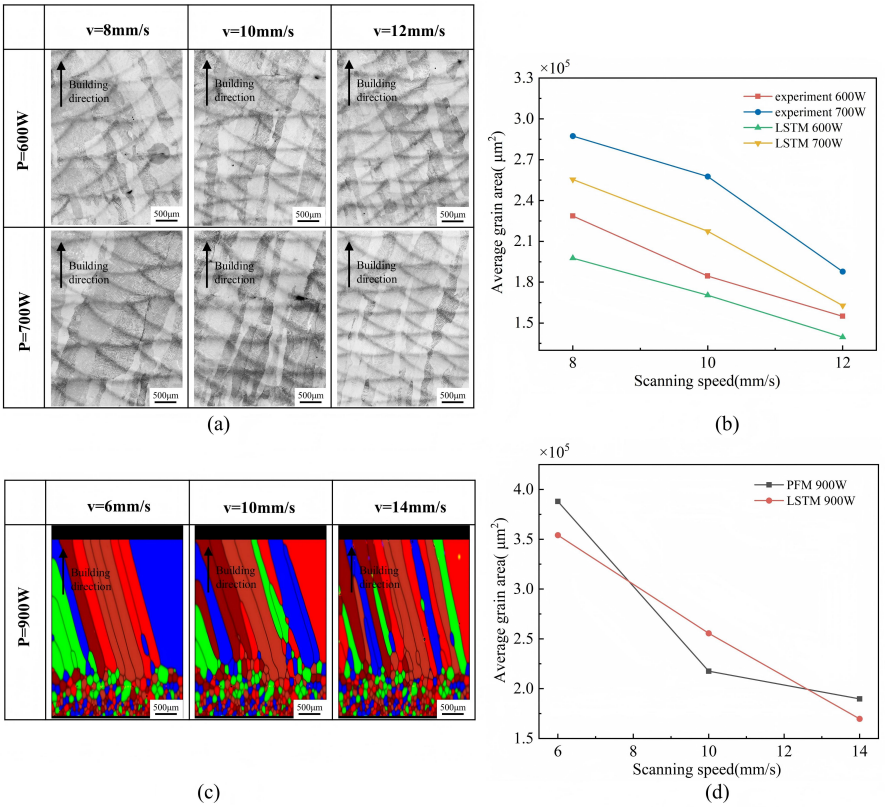

Figure 17. Validation of the proposed surrogate model through experimental measurements and extrapolation tests. **(a)** OM of six experimental samples on the x-z cross section; **(b)** Comparison between experimental and LSTM predicted average grain areas; **(c)** PFM microstructures under process conditions at 900 W on the x-z cross section; **(d)** Comparison between PFM and LSTM predictions for extrapolation assessment.

Table 6. Comparison of prediction accuracy for experimental validation and extrapolation assessment.

Model	R^2	RE	RMSE
Experimental validation	0.96	11.84%	13,710 μm²
Extrapolation	0.85	13.04%	33,915 μm²

To further evaluate the extrapolation capability of the proposed model beyond the training domain, additional grain growth simulations were performed using the PFM under a laser power of 900 W and scanning speeds of 6 mm/s, 10 mm/s, and 14 mm/s, as shown in Figure 17c.

As compared in Figure 17d, despite these processing conditions being completely excluded from the training dataset, the LSTM model reproduces the overall grain-growth trends. This extrapolation

assessment in Figure 6 yielded an R^2 value of 0.85, an RE of 13.04%, and an RMSE of 3.39×10^4 μm². The reduced prediction accuracy is primarily due to the fact that this process parameter is outside the training domain of the surrogate model. Under higher laser power conditions, the thermal history, heat accumulation behavior, and grain growth dynamics become increasingly nonlinear, resulting in a larger distribution shift between the training and extrapolation datasets. Consequently, the recursive forecasting uncertainty is amplified, leading to reduced extrapolation accuracy. Although the prediction accuracy is lower than that obtained for the LSTM cases, the model still captures the dominant process-microstructure relationships under unseen processing conditions.

A practical framework for the microstructure design of L-DED Ti-6Al-4V alloys was developed by integrating a surrogate model with experimental data and a physics-based model. The design objective was to obtain nearly equiaxed prior-β grains, which can improve the strength and toughness of additively manufactured Ti-6Al-4V components and reduce the risk of brittle fracture. Based on the preceding research in this study, the average grain area was selected as the primary indicator for tailoring the grain microstructure. To strictly ensure a high fraction of equiaxed morphologies and suppress the columnar-to-equiaxed transition (CET) limitations, the average grain width was introduced as a complementary criterion. Combined with the process window distribution diagram in Figure 15 and the corresponding grain morphological characteristics obtained from PFM, the typical grain size range under optimal process conditions is statistically summarized. To promote the formation of a higher fraction of near-equiaxed grains, the target region was defined as having an average grain area of less than 1.3×10^5 μm² and an average grain width of less than 125 μm. The resulting probability density distribution of near-equiaxed grains is presented in Figure 18, which illustrates the likelihood of obtaining near-equiaxed grains. The distribution clearly indicates that a laser power of 500–550 W combined with a scanning speed of 13–14 mm/s can maximize the suppression of excessive epitaxial columnar growth without post-process heat treatment. Without extensive experiments and computationally expensive simulations, the proposed dual-level data-driven framework enables efficient prediction of β grain evolution and rapid process optimization in L-DED Ti-6Al-4V. The developed methodology provides a promising route toward microstructure-informed process design and intelligent optimization of additively manufactured alloys.

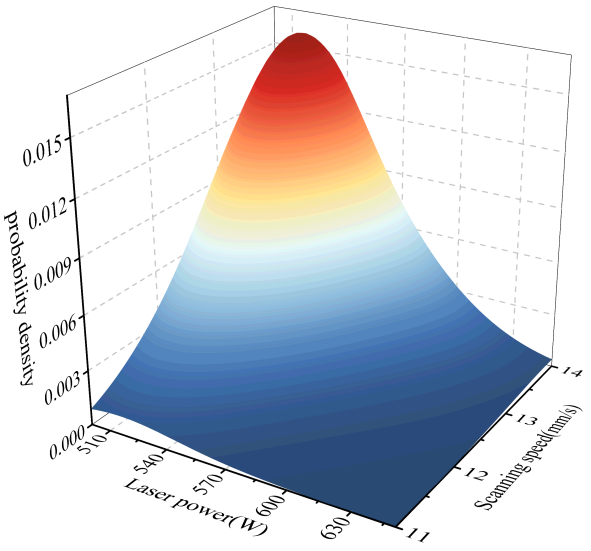

Figure 18. Probability density distribution of near-equiaxed grains in Ti-6Al-4V alloy under different process parameters.

5. Conclusion

In this study, a mechanism-data fusion framework was developed to predict the microstructural evolution of Ti-6Al-4V alloy fabricated via L-DED, integrating a finite element thermal model, a phase-field grain growth model, and a dual-level data-driven LSTM model. The main conclusions are as follows:

(1) The multiscale physical model reveals the grain growth mechanisms and the influence of process parameters on grain morphology. β grains evolve from equiaxed to columnar structures, driven by variations in thermal gradients and melt pool dynamics. Directional and epitaxial growth dominate this transition, promoting grain alignment along the deposition direction. Lower powers and higher speeds generally refine the grain structure by enhancing nucleation and suppressing epitaxial growth.

(2) The surrogate model demonstrates high fidelity and stabilization in mapping the non-linear temporal grain evolution in L-DED. Compared to the conventional MLP, the LSTM network effectively captures the time-dependent thermal accumulation. In recursive predictions, establishing four initial input layers as the optimal initialization length effectively captures layer-wise thermal accumulation and interlayer competitive grain growth. It achieved high prediction accuracy, with average R^2 values around 0.95, significantly outperforming the conventional MLP model. The framework effectively reduces layer-wise error accumulation during long-range predictions and provides reasonable predictions outside the training domain.

(3) Compared with multiscale physical simulations, the trained surrogate model can predict microstructures within a significantly reduced timeframe. By employing the average grain area as the primary microstructural control target and incorporating average grain width analysis, the parameter range of 500–550W and 13–14 mm/s was identified for achieving nearly equiaxed β grains.

Overall, the proposed framework provides a modular and extensible computational pipeline for coupling multiscale simulations with data-driven models. It enables efficient prediction of process-temperature-microstructure relationships and supports process parameter optimization in metal additive manufacturing. However, the current framework is established and validated within the investigated processing conditions and parameter ranges, and further validation under broader process windows is required to improve its general applicability.

Data availability statement

The data that support the findings of this study are available from the corresponding author upon reasonable request.

Declaration of generative AI and AI-assisted technologies

During the preparation of this manuscript, the authors used ChatGPT only for language polishing and improving readability. The authors take full responsibility for the content of the manuscript.

Acknowledgments

This work is financially supported by the National Natural Science Foundation of China (12202375), the Natural Science Foundation of Hebei Province (A2023203036). W.H. Yang is grateful for the financial support by the startup funds from the department of Mechanical Engineering at Prairie View A&M University.

Authors' contribution

Writing—original draft, Y.Zhang and T.Z.; writing—review and editing, Y.Zhang and P.L.; software, Y.Zhang and Y.Zhao; investigation, T.Z., X.W. and X.Z.; methodology, P.L., W.Y. and Z.W.; supervision, P.L. and X.L.; formal analysis, J.Y. and X.W.; funding acquisition, P.L. and W.Y. All authors have read and agreed to the published version of the manuscript.

Conflicts of interest

The authors declare that they have no known competing financial interests or personal relationships that could have appeared to influence the work reported in this paper.

References

[1] Svetlizky D, Das M, Zheng B, Vyatskikh AL, Bose S, *et al.* Directed energy deposition (DED) additive manufacturing: physical characteristics, defects, challenges and applications. *Mater. Today* 2021, 49:271–295.

[2] Ahmed N. Direct metal fabrication in rapid prototyping: a review. *J. Manuf. Process.* 2019, 42:167–191.

[3] Kaji F, Nguyen-Huu H, Narayanan JA, Zimny M, Toyserkani E. Intermittent adaptive trajectory planning for geometric defect correction in large-scale robotic laser directed energy deposition based additive manufacturing. *J. Intell. Manuf.* 2024, 35(7):3149–3168.

[4] Yan L, Chen Y, Liou F. Additive manufacturing of functionally graded metallic materials using laser metal deposition. *Addit. Manuf.* 2020, 31:100901.

[5] Liu Z, Jiang Q, Li T, Dong S, Yan S, *et al.* Environmental benefits of remanufacturing: a case study of cylinder heads remanufactured through laser cladding. *J. Clean. Prod.* 2016, 133:1027–1033.

[6] Si C, Wang S, Sun H, Feng Y. Constitutive relationship and deformation mechanism of SLM Ti-6Al-4V alloy under high strain rate. *J. Alloys Compd.* 2025, 1038:182659.

[7] Han Y, Cheng L, Zhao S, Zhang Y, Cheng Z, *et al.* In-situ study the distinct recrystallization pathways induced by boron and yttrium in Ti-6Al-4V. *J. Alloys Compd.* 2025, 1039:183130.

[8] Manoj A, Rao MA, Basha MM, Basha SM, Sankar MR. State of art on wire feed additive manufacturing of Ti-6Al-4V alloy. *Mater. Today Proc.* 2020, 26:2608–2615.

[9] Liu H, Bai X, Li Z, Fan L, Tang J, *et al.* Electrochemical evaluation of stress corrosion cracking susceptibility of Ti-6Al-3Nb-2Zr-1Mo alloy welded joint in simulated deep-sea environment. *Materials* 2022, 15(9):3201.

[10] Xiao Z, Wang W, Cui W, Qin G. Marine microbial corrosion inhibitation of an *in situ* formed oxide coating on Ti56Zr44 alloy. *Mater. Chem. Phys.* 2023, 304:127924.

[11] Paturi UMR, Palakurthy ST, Cheruku S, Vidhya Darshini B, Reddy NS. Role of machine learning in additive manufacturing of titanium alloys: a review. *Arch. Comput. Methods Eng.* 2023, 30(8):5053–5069.

[12] Jiang P, Li X, Zong X, Wang X, Chen Z, *et al.* Multi-wire arc additive manufacturing of Ti basic heterogeneous alloy: effect of deposition current on the microstructure, mechanical property and corrosion-resistance. *J. Alloys Compd.* 2022, 920:166056.

[13] Lu F, Ma Q, Liu E, Wei R, Bai J, *et al.* Advancements in understanding the microstructure and properties of additive manufacturing Ti-6Al-4V alloy: a comprehensive review. *J. Alloys Compd.* 2025, 1027:180543.

[14] Chen Y, Tan H, Fan W, Mi Z, Lin X, *et al.* Thermal behavior and microstructure of TC4-TA19 functionally graded materials by laser solid forming. *Foundry Technol.* 2022, 43(7):497–505.

[15] Guo C, Yin H, Chen W, Jiang F. Effects of ultrasonic vibration on mechanical properties and microstructure evolution of Ti-6Al-4V alloy manufactured by laser direct energy deposition. *Mater. Lett.* 2025, 393:138600.

[16] Wang C, Lei Y, Li C. Achieving an excellent strength and ductility balance in additive manufactured Ti-6Al-4V alloy through multi-step high-to-low-temperature heat treatment. *Materials* 2023, 16(21):6947.

[17] Khairallah SA, Martin AA, Lee JRI, Guss G, Calta NP, *et al.* Controlling interdependent meso-nanosecond dynamics and defect generation in metal 3D printing. *Science* 2020, 368(6491):660–665.

[18] Khairallah SA, Anderson AT, Rubenchik A, King WE. Laser powder-bed fusion additive manufacturing: physics of complex melt flow and formation mechanisms of pores, spatter, and denudation zones. *Acta Mater.* 2016, 108:36–45.

[19] Zadeh C, Stepanova T, Zarei A, Huang Y, Smith PM, *et al.* Establishing a process-structure-property-performance framework for SLS additive manufacturing through integrated multiscale modeling. *Mater. Des.* 2025, 257:114431.

[20] Ibrahimbegovic A, Niekamp R, Kassiotis C, Markovic D, Matthies HG. Code-coupling strategy for efficient development of computer software in multiscale and multiphysics nonlinear evolution problems in computational mechanics. *Adv. Eng. Softw.* 2014, 72:8–17.

[21] Zhang J, Liou F, Seufzer W, Taminger K. A coupled finite element cellular automaton model to predict thermal history and grain morphology of Ti-6Al-4V during direct metal deposition (DMD). *Addit. Manuf.* 2016, 11:32–39.

[22] Wang X, Liu P, Ji Y, Liu Y, Horstemeyer MH, *et al.* Investigation on microsegregation of IN718 alloy during additive manufacturing via integrated phase-field and finite-element modeling. *J. Mater. Eng. Perform.* 2019, 28(2):657–665.

[23] Kizhakkinan U, Duong PLT, Laskowski R, Vastola G, Rosen DW, *et al.* Development of a surrogate model for high-fidelity laser powder-bed fusion using tensor train and gaussian process regression. *J. Intell. Manuf.* 2023, 34(1):369–385.

[24] Xiao Y, Wang X, Yang W, Yao XX, Yang Z, *et al.* Data-driven prediction of future melt pool from built parts during metal additive manufacturing. *Addit. Manuf.* 2024, 93:104438.

[25] Bui NT, Ly KD, Dinh-Cong D, Nguyen-Thoi T. A multi-field coupled data-driven surrogate approach for multiphysical damage diagnostic of energy harvesting composite plates. *Adv. Eng. Softw.* 2025, 202:103871.

[26] Zavrakli E, Parnell A, Dickson A, Dey S. Data-driven linear quadratic tracking based temperature control of a big area additive manufacturing system. *J. Intell. Manuf.* 2025, 36(7):4549–4565.

[27] Tiwari K, Trivedi A, Reddy GB, Kumawat BK, Bhardwaj A, *et al.* Crystal plasticity modeling and data-driven approach for fatigue life estimation of additively manufactured Ti-6Al-4V alloy. *Int. J. Plast.* 2025, 189:104319.

[28] Ghungrad S, Haghighi A. Kinematics-guided data-driven energy surrogate model for robotic additive manufacturing. *Manuf. Lett.* 2024, 41:133–142.

[29] Luo H, He C, Xie H, He W, Ding C. AMBayes: a Bayesian data-driven framework for large-scale full-field prediction and process optimization with limited samples in additive manufacturing. *J. Intell. Manuf.* 2025.

[30] Chen S, Ding J, Shao Z, Shi Z, Lin J. An automated framework for optimising aluminium extrusion dies using data-driven surrogate models. *J. Intell. Manuf.* 2026.

[31] Doan VT, Massa F, Tison T, Naceur H. Coupling of homotopy perturbation method and Kriging surrogate model for an efficient fuzzy linear buckling analysis: application to additively manufactured lattice structures. *Appl. Math. Model.* 2021, 97:602–618.

[32] Wang Z, Yang W, Liu Q, Zhao Y, Liu P, *et al.* Data-driven modeling of process, structure and property in additive manufacturing: a review and future directions. *J. Manuf. Process.* 2022, 77:13–31.

[33] Sadeghpour E, Nonn A. Data-driven models for structure-property prediction in additively manufactured steels. *Comput. Mater. Sci.* 2022, 215:111782.

[34] Vulimiri PS, Riley S, Dugast FX, To AC. A mean–variance estimation bidirectional convolutional long short-term memory surrogate model predicting residual stress and model error for laser powder bed fusion. *Addit. Manuf.* 2025, 97:104591.

[35] Kamat S, Tucker V, Titus MS, Wagner GJ. A high-throughput physics- and data-driven framework for high-entropy alloy development. *Acta Mater.* 2025, 292:121045.

[36] Wang Z, Jiang C, Liu P, Yang W, Zhao Y, *et al.* Uncertainty quantification and reduction in metal additive manufacturing. *npj Comput. Mater.* 2020, 6(1):175.

[37] Li Y, Song L, Xie P, Cheng M, Xiao H. Enhancing hardness and wear performance of laser additive manufactured Ti6Al4V alloy through achieving ultrafine microstructure. *Materials* 2020, 13(5):1210.

[38] Smith J, Xiong W, Yan W, Lin S, Cheng P, *et al.* Linking process, structure, property, and performance for metal-based additive manufacturing: computational approaches with experimental support. *Comput. Mech.* 2016, 57(4):583–610.

[39] Liu P, Ji Y, Wang Z, Qiu C, Antonysamy AA, *et al.* Investigation on evolution mechanisms of site-specific grain structures during metal additive manufacturing. *J. Mater. Process. Technol.* 2018, 257:191–202.

[40] Boivineau M, Cagran CP, Doytier D, Eyraud V, Nadal MH, *et al.* Thermophysical properties of solid and liquid Ti-6Al-4V (TA6V) alloy. *Int. J. Thermophys.* 2006, 27(2):507–529.

[41] Brooks R, Robinson J, Chapman L, Richardson M. The enthalpy of a solid and liquid titanium-aluminium-vanadium alloy. *High Temp.-High Press.* 2003, 35–36(2):193–198.

[42] Junker D, Hentschel O, Schmidt M, Merklein M. Tailor-made forging tools by laser metal deposition. *Key Eng. Mater.* 2015, 651:707–712.
[43] Liu P, Wang Z, Xiao Y, Horstemeyer MF, Cui X, *et al.* Insight into the mechanisms of columnar to equiaxed grain transition during metallic additive manufacturing. *Addit. Manuf.* 2019, 26:22–29.
[44] Schempp P, Cross CE, Pittner A, Oder G, Neumann RS, *et al.* Solidification of GTA aluminum weld metal: part 1—grain morphology dependent upon alloy composition and grain refiner content. *Weld. J.* 2014, 93(2):53s–59s.
[45] Feng Y, He J, Han G, Li S, Lin Z. Deep learning predicting method and modeling of plastic constitutive relation of sheet metal (In Chinese). *J. Plast. Eng.* 2021, 28(6):34–46.
[46] He F, Yuan L, Mu H, Yang J, Ding D, *et al.* A recurrent neural network-based monitoring system using time-sequential molten pool images in wire arc directed energy deposition. *Mech. Syst. Signal Process.* 2025, 232:112733.
[47] Cortes G, Garcia-Suarez J. Data-driven dynamic friction models based on recurrent neural networks. *Appl. Comput. Geosci.* 2025, 26:100249.
[48] Qin Y, DeWitt S, Radhakrishnan B, Biros G. GrainNN: a neighbor-aware long short-term memory network for predicting microstructure evolution during polycrystalline grain formation. *Comput. Mater. Sci.* 2023, 218:111927.
[49] Mao H, Xie C, Pan J, Cao Q, Zhang X, *et al.* Spatiotemporal prediction of solidified dendrites based on convolutional long-short-term neural network. *Mater. Today Commun.* 2024, 41:110634.
[50] Kiran A, Kumar H, Sivanandam S, Senthilvel PG, Lalitha RVS, *et al.* Explainable AI in thermal modelling enhancing precision in thermal gradient monitoring for additive manufacturing using LSTM networks. *Therm. Sci. Eng. Prog.* 2025, 60:103465.
[51] Abdesselam KA, Gaudez S, Van Petegem S, Honkimäki V, Hallais S, *et al.* Altering microstructure and enhancing mechanical properties during direct energy deposition of Ti-6Al-4V via in-process laser heat treatments. *Mater. Des.* 2025, 254:113997.
[52] Shang C, Zheng J, Hou X, Jin K, Chu M, *et al.* Microstructure and tensile performance of Ti-1Al-8V-5Fe alloy produced by laser powder bed fusion *versus* directed energy deposition. *Vacuum* 2025, 234:114114.
[53] Zhang C, Liu F, Wang H. Effect of the prior-β grain boundaries on mechanical behavior of Ti6Al4V alloy processed by laser directed energy deposition. *Mater. Sci. Eng. A* 2022, 848:143389.
[54] Chen Z, Liu F, Chen J, Jiang G, Cui X, *et al.* Study on columnar-equiaxed crystal transition of laser deposited TC4 titanium alloy induced by synchronous layer-by-layer ultrasonic impact. *Mater. Sci. Eng. A* 2025, 931:148240.
[55] Al-Bermani SS, Blackmore ML, Zhang W, Todd I. The origin of microstructural diversity, texture, and mechanical properties in electron beam melted Ti-6Al-4V. *Metall. Mater. Trans. A* 2010, 41(13):3422–3434.
[56] Brandl E, Palm F, Michailov V, Viehweger B, Leyens C. Mechanical properties of additive manufactured titanium (Ti-6Al-4V) blocks deposited by a solid-state laser and wire. *Mater. Des.* 2011, 32(10):4665–4675.